

**Metal-insulator transition in  $(\text{Pr}, \text{Y})_{0.7}\text{Ca}_{0.3}\text{CoO}_3$  in the far-infrared spectral region**H. Němec <sup>\*</sup>, C. Kadlec , V. Goian, F. Borodavka , V. Železný, and M. Kempa   
*Institute of Physics ASCR, Na Slovance 2, 182 21 Prague 8, Czech Republic*K. Knížek  and J. Hejtmánek  
*Institute of Physics ASCR, Cukrovarnická 10, 162 00 Prague 6, Czech Republic*J. Buršík   
*Institute of Inorganic Chemistry ASCR, 250 68 Řež near Prague, Czech Republic*M. Soroka  
*Institute of Inorganic Chemistry ASCR, 250 68 Řež near Prague, Czech Republic  
and Charles University, Faculty of Science, Hlavova 2030/8, 128 43 Prague 2, Czech Republic* (Received 26 August 2020; revised 19 October 2020; accepted 20 October 2020; published 3 November 2020)

Bulk ceramics and thick nanogranular films of mixed-valence cobaltite  $(\text{Pr}_{1-y}\text{Y}_y)_{0.7}\text{Ca}_{0.3}\text{CoO}_3$  were studied using time-domain terahertz transmission spectroscopy and infrared reflection spectroscopy. Thanks to the high probing frequency, the overall increase in the conductivity during the insulator to metal transition was observed both in the ceramics and in the nanogranular films. The terahertz conductivity spectrum shows that the transition is not a simple cross-over between two states. As the charges become delocalized during the insulator to metal transition, a broad resonant mode corresponding to the eigenfrequency of the binding potential appears in the terahertz conductivity spectra in the ceramics, and it further softens as the metallic state prevails. This is interpreted as a consequence of the complexity of charge motion in a temperature-dependent energy landscape, changing dramatically from the tightly bound charges on atomic distance in the insulating phase to almost free charges in the metallic phase. This behavior is not directly observed in the nanogranular films as their nature introduces spectral signatures of an additional localization due to grain boundaries which obscure the pronounced effects observed in the bulk. Nevertheless fine spectral signatures accompanying the phase transition are still resolved. The insulator to metal transition is also accompanied by a weak softening of infrared-active phonon modes, which is related to the expansion of lattice parameters upon phase transition.

DOI: [10.1103/PhysRevB.102.195105](https://doi.org/10.1103/PhysRevB.102.195105)**I. INTRODUCTION**

Cobaltites include a wide group of materials in which strong electron correlations lead to a large diversity of their properties. A fine tuning of the material composition thus makes it possible to achieve a number of important functionalities, including superconductivity or metal-insulator phase transition. Their behavior is controlled especially by the mutual positioning of the  $t_{2g}$  and  $e_g$  energy levels [1]. The interplay between charge transport, localization, and magnetic ordering makes the phase diagrams of these materials particularly rich.

The  $\text{LaCoO}_3$ -type perovskites and structurally related compounds with variable  $\text{Co}^{3+/4+}$  valences are of fundamental interest, since the octahedrally coordinated cobalt ions can attain different electronic configurations, characterized as the low, high or intermediate spin states [2]. Such spin-state degree of freedom is at the root of the very complex and often contradicting behaviors with varying temperature and

material composition [3]. To shed light on these phenomena, numerous cobaltites were recently reinvestigated, mainly those where lanthanum was substituted by magnetic rare earths. This experimental and theoretical research included both the single valence  $\text{LnCoO}_3$  ( $\text{Ln} = \text{Pr}, \text{Nd}, \text{Sm}, \text{Tb}, \text{Dy}$ ) and mixed valence  $\text{Ln}_{1-x}\text{Ca}_x\text{CoO}_3$  ( $\text{Ln} = \text{Pr}, \text{Nd}$ ) systems (see, e.g., Refs. [4–8]). A special attention was paid to the peculiar metal-insulator transition found for the first time in the prototype calcium “half-doped”  $\text{Pr}_{0.5}\text{Ca}_{0.5}\text{CoO}_3$  and later on also in less doped systems like  $(\text{Pr}_{1-y}\text{Y}_y)_{0.7}\text{Ca}_{0.3}\text{CoO}_3$  (PYCCO). The transition is not due to a mere change in cobalt ions from the intermediate to the low-spin states, as previously speculated, but it is associated with a significant electron transfer between the  $\text{Pr}^{3+}$  and  $\text{Co}^{3+}/\text{Co}^{4+}$  sites [9–11]. This conclusion was also confirmed by x-ray absorption spectroscopy [12,13] and band structure calculations [14].

Charge transport is one of the most important processes which reflect the internal state of these materials, and it is also of fundamental interest in applications. The potential for applications may significantly grow when the materials can be prepared at low costs. It is thus essential to understand not only the behavior of high-quality (costly) materials, but also

<sup>\*</sup>nemec@fzu.cz

of nanogranular films which can be cheaply prepared using soft-chemistry methods like spin coating.

Terahertz (THz) spectroscopy is a method allowing noncontact probing of charge transport at nanometer distances [15,16], which makes it very suitable also for the investigation of polycrystalline materials. Furthermore, characteristic features in the THz conductivity spectra permit identification and disentanglement of various charge transport and response mechanisms [17], or understanding the potential landscape in which the charges move. Despite these benefits, the THz response of cobaltites has not been investigated systematically yet.

The metal-insulator phase transition in a number of correlated materials proceeds by nucleation of metallic domains [18,19]. This is a prominent example where the dc conductivity carries only a limited information: it steeply increases as the metallic domains become percolated, while the early stage of the formation of the metallic clusters (prior to the percolation) may be observed only in the high-frequency conductivity (e.g., THz). Measurements of the THz conductivity should bring a considerable insight into the processes in both poly- and nanocrystalline materials of this kind.

The experimental investigation of PYCCO family is complicated by the lack of good-quality bulk single crystals. Many samples are prepared in the form of thin layers. For example, high quality epitaxial films have been fabricated using pulsed laser deposition [20]. However, the lattice constant is largely mismatched with that of the substrate, which induces a compressive strain and thus modifies their properties. The strain also rapidly relaxes with the distance from the substrate [21], thus creating a gradient distribution of phase transition temperatures. Since the metal-insulator transition is accompanied by a strong lattice dilatation [11], the strain in the films generally depends on temperature, therefore it is practically impossible to disentangle the effects caused by the phase transition from those induced by the strain change [3,20].

In this view, it may be advantageous to work with nanogranular samples grown e.g. from chemical solution. The nanograins themselves are mechanically very stable, while the weakness of the mechanical coupling to the substrate as well as among themselves should release the strain inside individual nanograins. The drawback of this approach is that the commonly measured dc electrical conductivity then generally reflects contact resistance due to grain boundaries as well as intrinsic grain properties, and it may be difficult to distinguish these contributions [22]. The contact resistance in dense ceramics [10] may be lower, nevertheless similar arguments still apply.

These issues may be resolved using a measurement of high-frequency conductivity spectrum, which typically reflects the motion of charges on distances corresponding to the diffusion length during a period of the probing radiation [22,23]. Charge transport over nanometer distances thus can be typically probed using terahertz (THz) frequencies [24]. Despite an important progress in the past years, a microscopic interpretation of THz conductivity spectra of nanostructures remains a challenge. One needs to consider at least two effects, which often have a similar influence on the conductivity spectra [16]:

(1) Distribution of the probing electric field may be strongly affected by depolarization fields resulting from the system heterogeneity, which implies that the effective (measured) conductivity differs from the conductivity of the constituting nanostructures [25]. The effect is reduced to a simple scaling in the case of percolated systems, and to the development of plasmonic resonance in the nonpercolated ones [26,27]. Dense materials like the nonporous ceramics and the good-quality films studied in this manuscript are percolated, therefore plasmonic effects are not an issue here.

(2) THz conductivity spectra are controlled by the landscape of the potential in which the charges move. In particular, confinement of the charge motion within an infinite rectangular potential well (representing the confinement of charges inside nanograins) generally shifts the spectral weight from the zero frequency (Drude peak) toward higher frequencies [24,28]. But also a smooth modulation of the potential plays an important role: Charges spend most of the time close to the potential minima and the corresponding eigenfrequencies manifest themselves as resonances in the THz conductivity spectra [29]. We anticipate that changes in the potential energy landscape accompany the metal-insulator phase transition in PYCCO. Measurement of THz conductivity spectra then provides information about the potential landscape and its evolution with temperature.

In this article, time-domain THz spectroscopy is combined with reflection Fourier-transform infrared spectroscopy. The resulting broad spectral range permits a detailed study of charge transport properties and the behavior of the lattice from the dynamics of phonon modes.

## II. SAMPLES AND EXPERIMENTAL SETUPS

Complex terahertz conductivity spectra in the spectral range 0.2–2.5 THz were measured in a common homemade setup for time-domain transmission THz spectroscopy equipped with a helium-flow cryostat [30]. Most measurements were performed in a mode with continuous temperature variation, with a rate not exceeding 2 K per minute. This ensures that the temperature change during the measurement of each waveform is significantly smaller than 1 K, which we consider as the accuracy of the temperature determination.

Infrared power reflectivity in the spectral range 4–18 THz was measured using a Fourier spectrometer Bruker IFS113v. The temperature in a helium-flow cryostat was stabilized prior to the measurement; as a consequence, only a few spectra at a set of discrete temperatures were measured. There is no way to unambiguously retrieve the complex optical properties from the power reflectivity. Since Kramers-Kronig analysis may provide inexact results due to the limited spectral range [31], we prefer to calculate the reflectivity spectra from model permittivity spectra.

Microwave response at 6.7 GHz was measured using the composite dielectric resonator method [32–34]. The  $TE_{018}$  resonance frequency, quality factor and insertion loss of the base cylindrical dielectric resonator with and without the sample were recorded during heating from 10 to 400 K with a temperature rate of 0.5 K/min in a Janis closed-cycle He cryostat. Half-millimeter thick plates without electrodes (bare fused silica substrate and substrate with the PYCCO film)

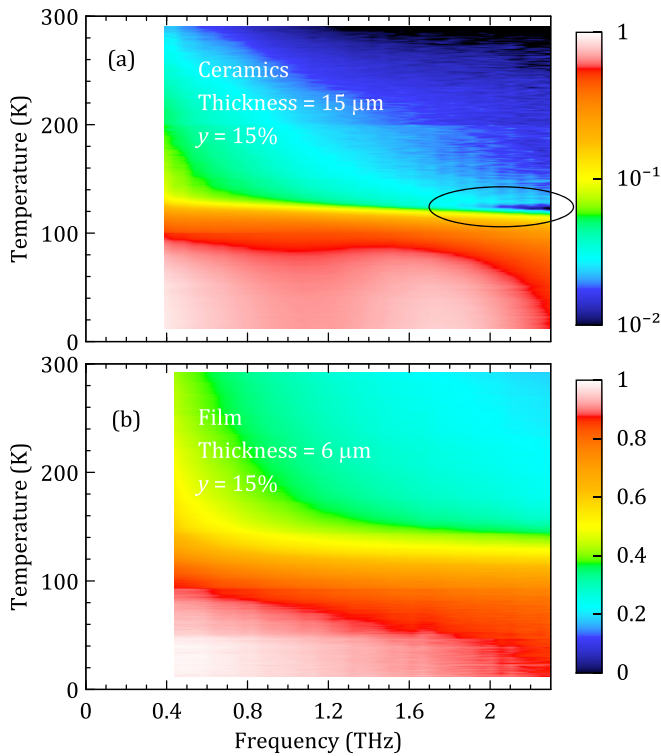


FIG. 1. Amplitude of the measured transmittance spectra (ratios of electric field intensities)  $\mathcal{T}$  of the (a) 15  $\mu\text{m}$  thick ceramics and (b) 6  $\mu\text{m}$  thick nanogranular film. These graphs demonstrate that both samples are always transparent enough ( $\mathcal{T} > 1\%$ ) to enable accurate transmittance measurement, and interacting with the THz radiation strongly enough to permit reliable retrieval of optical characteristics ( $\mathcal{T}$  is less than 95% except for a small area at low temperatures and low frequencies). Note that accurate transmittance phase is available in the entire range. The ellipse in panel (a) indicates a region with a sharp dip in temperature dependence, which will be discussed later.

were placed on top of the base resonator. The resonators were measured in the cylindrical shielding cavity using the transmission setup with a weak coupling with the Agilent E8364B network analyzer. Dielectric parameters of the samples were calculated from the measured resonance frequencies and quality factors of the base and composite resonators.

The atomic force microscopy (AFM) measurements were conducted using the AFM microscope of the NTEGRA Spectra apparatus operated with silicon cantilevers in a contact mode.

The metal-insulator transition is accompanied by a considerable variation of THz conductivity and therefore also by a substantial change of THz transmittance, which imposes important constraints on the measurement strategy. In particular, the thickness of the samples has to be selected carefully: thick samples permit accurate characterization of the insulating state, but they are completely opaque in the metallic phase; thin samples allow straightforward investigation of the metallic state but the characteristics of the insulating state are highly inaccurate due to the short interaction pathway of the THz radiation with the sample. Optimum thicknesses in our case span from a few microns to  $\sim 25 \mu\text{m}$  (Fig. 1), which requires

special preparation of the samples. In principle, one could think about measurements in reflection geometry. However, retrieval of optical properties from reflectance measurements is over-sensitive to the mutual positioning of the sample and the reference mirror [35]. Although a few highly specific and reasonably accurate methods have been developed and applied at room temperature (Ref. [35] and references therein), it would be too difficult to extend them for cryostat operation, particularly in conjunction with continuous temperature sweep.

Thick films of  $(\text{Pr}_{1-y}, \text{Y}_y)_{0.7}\text{Ca}_{0.3}\text{CoO}_3$  were prepared by chemical solution deposition method. Metal 2-ethylhexanoates [in-house synthesized  $\text{Pr}(\text{O}_2\text{CH}(\text{CH}_2\text{CH}_3)(\text{CH}_2)_3\text{CH}_3)_3$ ,  $\text{Y}(\text{O}_2\text{CH}(\text{CH}_2\text{CH}_3)(\text{CH}_2)_3\text{CH}_3)_2$ ,  $\text{Ca}(\text{O}_2\text{CH}(\text{CH}_2\text{CH}_3)(\text{CH}_2)_3\text{CH}_3)_2$ , and commercial  $\text{Co}(\text{O}_2\text{CH}(\text{CH}_2\text{CH}_3)(\text{CH}_2)_3\text{CH}_3)_2$  from ABCR Germany] were used as metal precursors, iso-butanol and 2,2-diethanolamine [DEA,  $\text{NH}(\text{CH}_2\text{CH}_2\text{OH})_2$ ] were used as solvent and modifier in synthesis of deposition solutions. After the deposition using a spin coating technique the gel films were dried and pyrolysed at  $300^\circ\text{C}$  for 5 min, followed by heat treatment at  $800^\circ\text{C}$  for 15 min in a preheated tube furnace. To obtain the desired film thickness the deposition-annealing cycle had to be repeated more times (typically with 200 nm per one cycle). The final crystallization annealing was done at  $900^\circ\text{C}$  for 24 h in the atmosphere of flowing oxygen. One batch of  $\sim 6 \mu\text{m}$  thick films with different compositions ( $y \in \{0, 6\%, 10\%, 15\%\}$ ) was deposited on *c*-cut sapphire substrates. In another batch,  $\sim 4 \mu\text{m}$  thick films with composition  $y = 16\%$  were deposited on sapphire and fused silica substrates. The phase composition was verified using x-ray diffraction patterns.

Handling of thin ceramics is even more delicate due to the fragility. For this reason, a piece of bulk ceramics with  $y = 15\%$  (identical material as that studied in Ref. [10]) was glued to a *c*-cut sapphire substrate to form an optical contact, and mechanically thinned down to the thickness of 15  $\mu\text{m}$ ; the ceramics remained attached during the THz measurements. For the retrieval of the terahertz conductivity, we considered all interferences in the thin ceramics, similarly as in the case of optically thin films [36]. We also verified that the influence of the optical contact on the retrieval procedure is negligible.

### III. TERAHERTZ CONDUCTIVITY

#### A. Modified Drude-Smith model

Intraband transport of free charges in most bulk semiconductors and metals is usually understood in terms of the Drude model, which assumes that a free motion of charges is interrupted by scattering events, occurring with the mean momentum relaxation time  $\tau$ . The conductivity spectrum then follows the Drude formula [37]

$$\sigma(f) = \frac{\sigma_{\text{dc}}}{1 - 2\pi if\tau}, \quad (1)$$

which is characterized by a decrease of the real part of conductivity with frequency.

This picture changes when the motion of these free charges is additionally confined into grains, nanoparticles or other submicron sized nanoobjects. On a microscopic

level, the response has been recently described both quantum-mechanically and semiclassically [24,28,30,38]. Here we will take advantage of the modified Drude-Smith model developed by Cocker *et al.* [28], which is an analytical expression with intuitive interpretation:

$$\sigma(f) = \frac{\sigma_1}{1 - 2\pi i f \tau_1} \left( 1 + \frac{c_1}{1 - 2\pi i f \theta_1} \right). \quad (2)$$

The parameter  $c_1$  describes the degree of back-scattering of charges at grain boundaries. Perfectly reflecting boundaries are represented by  $c_1 = -1$  and they completely suppress dc conductivity [ $\sigma(f=0) = 0$ ]. Absence of boundaries is equivalent to  $c_1 = 0$ ; the second term in Eq. (2) then vanishes and the equation thus reduces to the Drude response [Eq. (1)]. The major difference compared to the phenomenological Drude-Smith model [39] is the new time  $\theta_1$ , which is a characteristic diffusion time inside the grains. For large enough grains (scattering of charges in the bulk is more frequent than interaction with grain boundaries,  $\tau_1 \ll \theta_1$ ),  $\tau_1$  keeps the meaning of the mean scattering time from the Drude model,  $\sigma_1$  approaches the dc Drude conductivity, and  $\theta_1 = L^2/(12D)$  where  $L$  is the grain size and  $D$  is the diffusion coefficient of charges. Substituting for the diffusion coefficient of a degenerate Drude electron gas in a parabolic band,  $D = v_F^2 \tau_1/3$ , we obtain

$$\theta_1 = \frac{1}{\tau_1} \left( \frac{L}{2v_F} \right)^2, \quad (3)$$

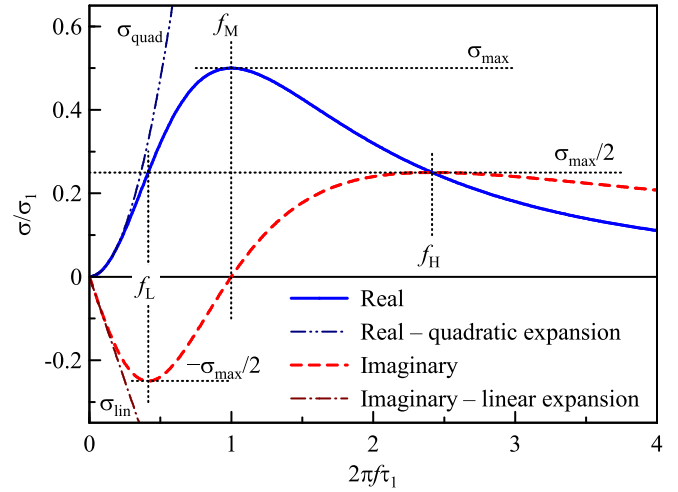
i.e.,  $\theta_1$  reflects not only the grain size  $L$ , but also the Fermi velocity  $v_F$  and the carrier scattering time  $\tau_1$ .

Since Eq. (2) will be used for extensive fitting, it is useful to know the basic characteristics of its graph, particularly in the important limit  $c_1 \rightarrow -1$  (Fig. 2). For simplicity, we will further assume the regime of larger grains in which charges are more scattered in the grain interior than by grain boundaries (formally expressed by the condition  $\tau_1 \leq \theta_1$ ). A straightforward analysis provides the following basic properties and rules controlling the reliability of determination of individual parameters from a fit:

(1) Reliable determination of the amplitude  $\sigma_1$  requires observation of the maximum in the real part of conductivity; then  $\max(\text{Re } \sigma) = \sigma_1 \theta_1 / (\theta_1 + \tau_1)$  which provides in most cases the amplitude  $\sigma_1$  accurately.

(2) The minimum in the imaginary part occurs at a frequency  $(\sqrt{\tau_1^2 + \theta_1^2} + 6\tau_1\theta_1 - \tau_1 - \theta_1)/(2\tau_1\theta_1)$ ; its position is thus controlled predominantly by the larger of the values  $\tau_1$  and  $\theta_1$ . Observation of a minimum in the imaginary part thus permits accurate determination of the diffusion time  $\theta_1$  in our case. Alternatively, the product  $\sigma_1\theta_1$  can be estimated from the initial slope in the imaginary part since  $\sigma|_{f \rightarrow 0} = -2\pi i f \theta_1 \sigma_1$ .

(3) The crossing of the real and imaginary part occurs at the same frequency as the maximum in the imaginary part,  $(\sqrt{\tau_1^2 + \theta_1^2} + 6\tau_1\theta_1 + \tau_1 + \theta_1)/(2\tau_1\theta_1)$ ; this frequency is thus controlled mainly by the smaller of the values  $\tau_1$  and  $\theta_1$ . Observation of the crossing thus permits accurate determination of the scattering time  $\tau_1$  in our case. Alternatively, the ratio  $(\text{Im } \sigma / \text{Re } \sigma)|_{f \rightarrow \infty} = 2\pi f \tau_1 \theta_1 / (\tau_1 + \theta_1)$  also provides information on the smaller of the times.



$$\begin{aligned} 2\pi f_L &= \frac{\sqrt{\tau_1^2 + \theta_1^2} + 6\tau_1\theta_1 - \tau_1 - \theta_1}{2\tau_1\theta_1} \sim \frac{3}{2\theta_1} \\ 2\pi f_M &= \frac{1}{\sqrt{\tau_1\theta_1}} \\ 2\pi f_H &= \frac{\sqrt{\tau_1^2 + \theta_1^2} + 6\tau_1\theta_1 + \tau_1 + \theta_1}{2\tau_1\theta_1} \sim \frac{1}{\tau_1} \\ \frac{\sigma_{\max}}{\sigma_1} &= \frac{\theta_1}{\theta_1 + \tau_1} \sim 1 \\ \frac{\sigma_{\min}}{\sigma_1} &= -2\pi i f \theta_1 \\ \frac{\sigma_{\text{quad}}}{\sigma_1} &= 4\pi^2 f^2 \theta_1 (\tau_1 + \theta_1) \sim (2\pi f \theta_1)^2 \end{aligned}$$

FIG. 2. Illustration of the modified Drude-Smith model [Eq. (2)] in the specific case  $c_1 = -1$  and identification of important points of its graph. The expressions following the  $\sim$  sign apply for  $\tau_1 \ll \theta_1$ .

If a particular extreme of the function is not observed in the spectra, the accuracy of the corresponding control parameter may be significantly compromised as it relies on the extrapolation of possibly subtle details of the spectrum and may be thus accompanied by substantial correlations with other model parameters.

For low frequencies, the real part of the conductivity is a parabola  $\sigma_1(1 + c_1) - 4\pi^2 f^2 \sigma_1 [\tau_1^2 + c_1(\tau_1^2 + \tau_1\theta_1 + \theta_1^2)]$ . Reliable determination of  $\sigma_1$  together with observation of the bottom of this parabola in the low-frequency region of the real part of conductivity is thus a prerequisite for an accurate characterization of  $c_1$ . Note also that for  $c_1$  close to 0, the term containing the diffusion time  $\theta_1$  becomes marginalized, i.e., accurate determination of  $\theta_1$  from the fit becomes no longer possible (the parameters  $\theta_1$  loses its sense).

## B. Terahertz conductivity of bulk ceramics

In a global overview of the THz conductivity spectra of the 15  $\mu\text{m}$  thick ceramics ( $y = 15\%$ ) [Fig. 3(a)] we can clearly distinguish both the insulating and metallic regime. In the insulating phase (temperatures below  $\sim 100$  K), the real part of the conductivity is small and the imaginary part decreases, which is a manifestation of nondispersive background permittivity. In the metallic regime (temperatures above  $\sim 140$  K), the real part of the conductivity decreases with increasing

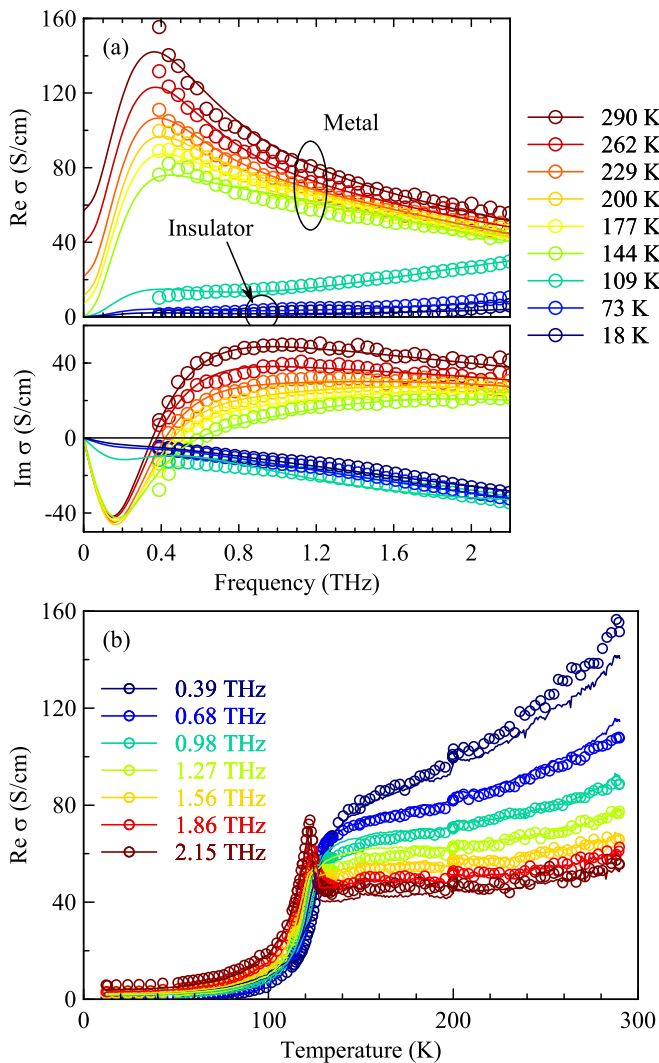


FIG. 3. Global overview of the THz conductivity spectra of the 15 μm thick PYCCO ceramics ( $y = 15\%$ ). Symbols: measured data, lines: fit using Eq. (4).

frequency and the imaginary part is mainly positive, thus resembling to the Drude response [Eq. (1)].

A closer inspection reveals a pronounced enhancement of the real part of the conductivity for frequencies above 1.5 THz in the vicinity of 120 K [Fig. 3(b); see also Fig. 1 where the conductivity enhancement appears as a clear dip in the transmittance]. The nonmonotonous behavior in the temperature dependence is in fact a principal result demonstrating that the phase transition is not a simple cross-over from one state to another. Instead, the transition is accompanied by an excitation active in the THz spectral region with a spectral shape continuously evolving with temperature.

A more detailed view (Fig. 4) shows that the THz conductivity spectra around 120 K include an additional broader resonance, blue-shifting from 1.9 THz at 125 K above 2.2 THz (the upper limit of the accessible spectral range) for  $T \lesssim 121$  K.

Note also that even the response in the metallic phase somewhat deviates from the Drude conductivity. In particular, the imaginary part of conductivity crosses (or has a

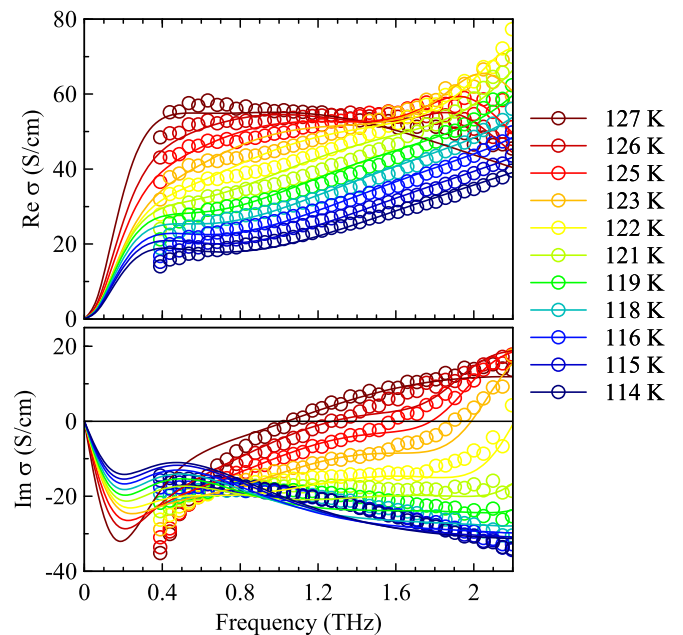


FIG. 4. A detailed graph of the THz conductivity spectra of the 15 μm thick PYCCO ceramics ( $y = 15\%$ ) in the vicinity of the phase transition. Symbols: measured data, lines: fit using Eq. (4).

tendency to cross) zero at low frequencies; with regard to Kramers-Kronig relations, this implies that the real part of the conductivity has to decrease with decreasing frequency below the accessible spectral range ( $\sim 0.4$  THz). These are signatures of charge localization. Although no clear internal structure can be seen in atomic force microscopy image of the ceramics (Fig. 5), it is probable that grain boundaries are responsible for this behavior.

To explain the behavior of the conductivity spectrum, we formally decompose it into two modified Drude-Smith terms  $\Sigma_1$  and  $\Sigma_2$  (accounting for the band transport combined with confinement inside the grains) and one oscillator term  $\Sigma_{osc}$

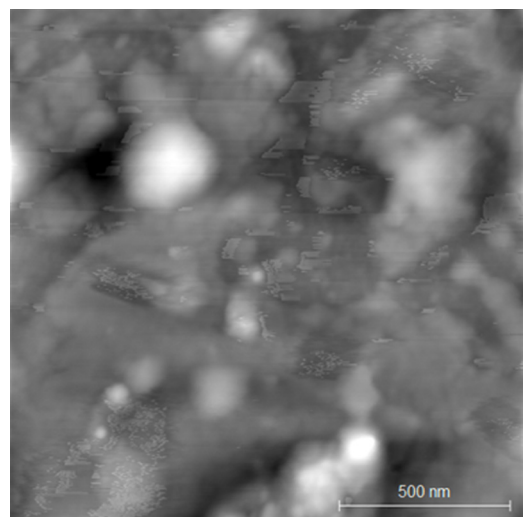


FIG. 5. Atomic force microscopy image of the surface of the PYCCO ceramics ( $y = 15\%$ ).

(with eigenfrequency  $f_{\text{osc}}$ , damping  $\gamma_{\text{osc}}$  and amplitude  $\sigma_{\text{osc}}$ ) representing the additional spectral feature resolved close to 120 K:

$$\sigma(f) = \Sigma_1(f) + \Sigma_2(f) + \Sigma_{\text{osc}}(f) + \Sigma_p(f), \quad (4)$$

where

$$\begin{aligned} \Sigma_k(f) &= \frac{\sigma_k}{1 - 2\pi i f \tau_k} \left( 1 + \frac{c_k}{1 - 2\pi i f \theta_k} \right), \\ \Sigma_{\text{osc}} &= \sigma_{\text{osc}} \frac{-i f \gamma_{\text{osc}}}{f_{\text{osc}}^2 - f^2 - i f \gamma_{\text{osc}}}, \\ \Sigma_p &= -2\pi i f \varepsilon_p \varepsilon_0. \end{aligned}$$

We also have to account for the permittivity  $\varepsilon_p$  of the lattice, which is represented by the conductivity term  $\Sigma_p$ .

For each temperature, this general model involves 12 parameters for fitting one complex conductivity spectrum, which is obviously an overkill. To reduce the number of parameters, we performed a global fit involving all temperatures where we considered selected parameters as temperature independent. A good quality of the fit was achieved for temperature-independent  $\varepsilon_p$ ,  $\sigma_1$ ,  $c_2$ ,  $\tau_2$ ,  $\theta_2$  and  $\gamma_{\text{osc}}$ ; furthermore, it was found that  $\theta_1 = \tau_1$  which leaves us with five fitting parameters to fit a complex spectrum per each temperature (when the oscillator term is present) and with three when the oscillator term vanishes.

The fitting parameters are summarized in Fig. 6; the quality of the fits can be assessed in Figs. 3 and 4. The spectra corresponding to individual terms in Eq. (4) are illustrated in Fig. 7.

### 1. Formal interpretation of the fitting model

To get the first insight into the interpretation of the results of the fits we discuss the behavior of the components in the fitting model [Eq. (4)]. We emphasize that this is just a model phenomenologically describing the spectra. A model with a physical interpretation will be developed and discussed in the next subsection.

In the following discussion, we should consider the findings of Sec. III A: The accurately determined parameters describing the metallic state are  $\sigma_k$  (the maximum in the conductivity is almost reached) and  $\tau_k$  (decrease of conductivity with frequency is resolved), whereas  $\theta_k$  and  $c_k$  are less accurate. In the insulating state, it is namely the  $\sigma_k \theta_k$  product which is determined accurately.

From the temperature dependence of the  $\sigma_2$  amplitude, we can clearly assess that it is the  $\Sigma_2$  which is closely associated with the phase transition. This term also significantly contributes to the Drude-like shape of the spectra in the metallic state (Fig. 7) with a rather long scattering time ( $\tau_2 = 0.44$  ps). Note also that this parameter is determined reliably since we have an access close to the frequency where the real and imaginary part of the conductivity cross. The progressive increase in  $\sigma_2$  with temperature then indicates the essence of the insulator to metal transition: the growth in the population of free charges, with the most rapid change around 120 K. The resulting value of the  $c_2 = -1$  would—strictly speaking—signify an absence of a long-range (dc) transport. However, the accuracy of this coefficient is rather

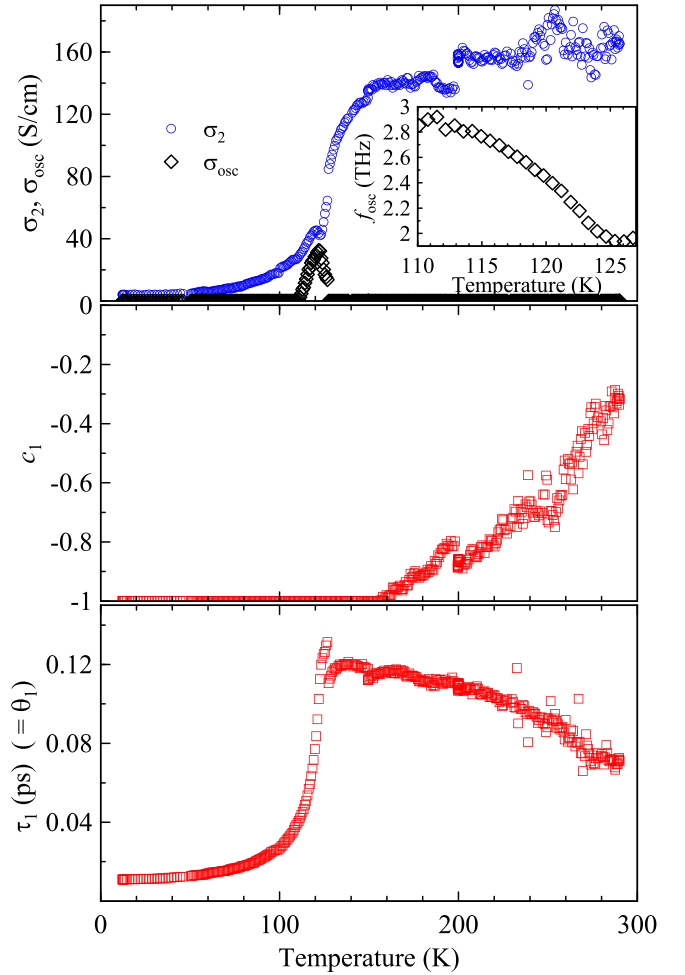


FIG. 6. Temperature dependence of the fitting parameters in Eq. (4). Global fitting parameters (common for all temperatures) are  $\sigma_1 = 86$  S/cm,  $c_2 = -1$ ,  $\tau_2 = \theta_2 = 0.44$  ps,  $(2\pi\gamma_{\text{osc}})^{-1} = 0.23$  ps,  $\varepsilon_p = 14$ .

poor (the value is controlled namely by the behavior of the spectra below the accessible spectral range); a small deviation from  $-1$  may then cause the weak dc conductivity observed previously [10].

The behavior of the  $\Sigma_1$  term is more complex as its spectral shape evolves with temperature. Its contribution to the conductivity in the insulating state is marginal, as the scattering time  $\tau_1$  is short and the back-scattering coefficient  $c_1$  equals to  $-1$ . During the phase transition, the scattering time  $\tau_1$  suddenly increases and also the back-scattering coefficient  $c_1$  starts to increase, resulting in an important contribution of the  $\Sigma_1$  term to the Drude-like conductivity spectra.

Finally, there is a very narrow temperature region around 120 K where a contribution from an oscillator appears. By a close inspection of the spectra in Fig. 4 we can confirm that this feature is not an artifact: for example, a rapid increase in  $\text{Re } \sigma$  is observed at 122 K, and a subtle but clear maximum is observed at 125 K, both of them being clear signatures of a distinguished oscillatorlike response. The oscillator eigenfrequency decreases with increasing temperature.

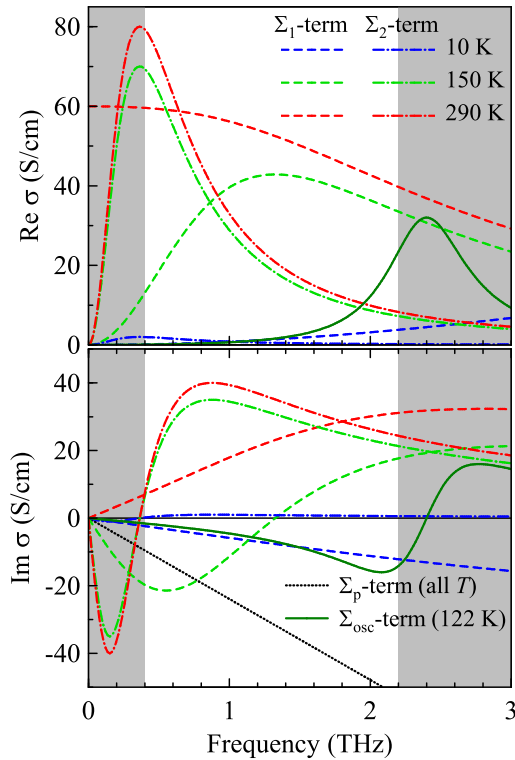


FIG. 7. Spectrum of individual terms in Eq. (4). The gray areas indicate spectral ranges not accessible experimentally.

## 2. Physical interpretation of the fitting model

Although the formal interpretation of the spectra provides an important first insight, it contains a number of controversial issues (puzzling behavior of both of the terms  $\Sigma_1$  and  $\Sigma_2$ , absence of long-range conductivity, narrow region with a pronounced oscillator response). We thus need to rethink the assignment and the actual spectral response of the real underlying excitations.

We start with the insulating state (10 K), where the response is essentially dominated by the phonon permittivity  $\epsilon_p$  and somewhat affected by the  $\Sigma_1$  term, while the contribution of the  $\Sigma_2$  term and the oscillator term is negligible. Since the characteristic times  $\tau_1$  and  $\theta_1$  are very short, the corresponding spectral response of the  $\Sigma_1$  term reduces to  $\approx -2\pi if\sigma_1\theta_1(T)$ . Note however, that this response is spectrally indistinguishable from the term  $-2\pi if\epsilon_p\epsilon_0$  due to the lattice permittivity. A simpler explanation is that the insulating state is characterized solely by a temperature-dependent permittivity  $\epsilon(T) = \epsilon_p + \sigma_1\theta_1(T)/\epsilon_0$ . This permittivity then slightly increases with increasing temperature as a result of the temperature dependence of  $\theta_1(T)$ . In terms of Lyddane-Sachs-Teller relation [40], this behavior may be associated with softening of phonon modes, which was indeed observed in the infrared spectra in Sec. IV.

In the metallic phase (300 K), the oscillator term  $\Sigma_{\text{osc}}$  is negligible whereas the contributions of both modified Drude-Smith terms have a comparable magnitude, and—at least in the accessible THz range—a qualitatively Drude-like character. It is thus probable that the formal  $\Sigma_1$  and  $\Sigma_2$  terms together represent a single broader excitation with a peak

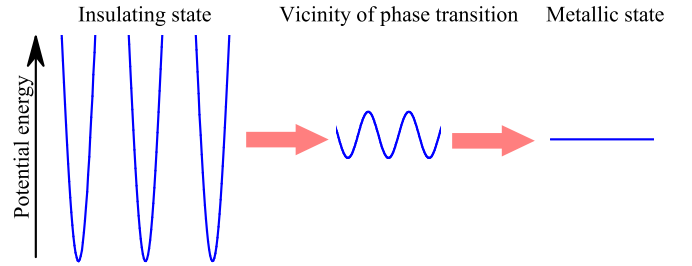


FIG. 8. Scheme of potential landscape evolution during the insulator to metal transition in yttrium-doped PYCCO. At low temperatures (insulating state), charges are localized on atomic distances in deep potential wells. Upon the phase transition, the potential modulation depth fundamentally decreases, thus permitting a long-range charge transport, but still keeping certain signatures of charge localization. In the metallic state, the potential modulation disappears and the charges are moving freely.

below 0.4 THz, which is at the same time responsible for the long-range (dc) conduction. On a qualitative level, this feature can be understood in terms of frequency-dependent scattering time [31,41]. As the temperature decreases, the degree of localization is enhanced (and thus the long-range transport suppressed), as evidenced in the back-scattering parameter  $c_1$  in the  $\Sigma_1$  term decreasing to  $-1$ . This behavior also explains that the amplitude of this excitation (represented by the sum  $\sigma_1 + \sigma_2$ ) does not change significantly in the entire metallic state, whereas the dc resistance somewhat increases with decreasing temperature [10].

The increasing degree of localization has to be accompanied by a blue shift of the spectrum associated with the charge response [24]. This behavior indeed occurs in the sum of the  $\Sigma_1$  and  $\Sigma_2$  terms, as a consequence of the decrease of the back-scattering coefficient  $c_1$ : A very broad maximum appears around 0.6 THz for  $T = 127$  K (Fig. 4), being still caused solely by the sum of the  $\Sigma_1$  and  $\Sigma_2$  terms. For even lower temperatures, the maximum further blue-shifts and the resonance becomes more pronounced: this is the reason why we need the additional oscillator term in this narrow temperature region. In other words, we observe that the oscillatorlike response does not appear/disappear suddenly. We interpret this fact as that the excitation underlying the phase transition is a rather broad mode blue-shifting with temperature, which manifests a degree of localization of charge carriers continuously changing with temperature.

The anticipated entire behavior is schematically illustrated in Fig. 8. Charges in the insulating state are bound in deep narrow potential wells, providing no response in the THz spectral range. With approaching phase transition, the wells become shallower: long-term transport starts to be enabled thermally, and the eigenfrequency near the potential well minimum decreases. Finally, the charges move (almost) freely in the metallic state.

Note also that the nature of the metallic phase itself is rather complex. We observed two signatures of a classical metallic behavior: (i) THz conductivity spectra show a clear Drude-like peak associated with the intraband motion of charges, and (ii) the observed decrease of the carrier scattering time  $\tau_1$  in (Fig. 6) with increasing temperature should

reflect enhanced charge-phonon scattering. However, at the same time both dc [10] and THz conductivities increase with increasing temperature, which is rather a signature of semi-conducting behavior. Together, this means that new charges are being released with increasing temperature, which may indicate a continuing progressive delocalization of charges even far above the phase transition temperature.

Independently of the chosen fitting model, the very rapid decrease of the real part with frequency unambiguously describes some relaxation processes with rather long characteristic times. In the formal fitting model, we resolved the scattering time  $\tau_2$  as long as 0.44 ps; in reality, the sense of the small systematic deviations of the fit from the measured conductivity at the lowest frequencies (Fig. 3) indicates that components with even longer characteristic times are present. These are extraordinarily long time, given the “dirty” nature of the ceramics, presence of grain boundaries, and room temperature promoting the scattering by phonons [for comparison, scattering time in a good-quality silicon at room temperature is  $\sim 0.25$  ps [42)]. From the amplitude of the conductivity, we can deduce that only a very small fraction (less than 1%) of available free charges induced by the doping are exhibiting such a long scattering time. A similar behavior (long scattering times exhibited by a tiny fraction of available charges) was observed by us in a much more disordered thin layer of  $\text{Na}_{0.63}\text{CoO}_2$  and attributed to trapping of charges in deep traps [43]. However, since this behavior is now observed in a much “cleaner” system, it seems that it is a more general property of charge transport in doped cobalt-based oxides requiring a different explanation. If the majority of charges exhibited extremely short scattering times, their response in the THz conductivity spectra would be marginal. A smooth connection of these “majority” and “minority” charges may be done by considering the frequency-dependent scattering time [31]. This explanation opens two intriguing questions: why certain charges are scattered so inefficiently despite the nature of the material and why the frequency dependence starts becoming important already at sub-THz frequencies.

### C. Role of the grain size in nanogranular films

Atomic force microscopy images of the surface of PYCCO films reveal different grain sizes when deposited on fused silica and sapphire substrates [Figs. 9(a)–9(c)]. The shape of the THz conductivity spectra of these films in the metallic phase [Fig. 9(d)] also differs from each other. More importantly, there is a fundamental qualitative difference compared to the spectra of the ceramics with a similar phase composition [Fig. 3(a)].

We attribute the change in the spectral shape to the localization of charges by grain boundaries. The size of the grains on the sapphire substrate is by about 20% larger than on the fused silica substrate. Indeed, the characteristic diffusion time  $\theta_1$  obtained from the fit by the modified Drude-Smith model [Fig. 9(d)] is considerably shorter for the film on the fused silica substrate, thus reflecting the role of the size effect through Eq. (3). To further confirm the consistency of these considerations, we estimate the scattering time  $\tau_1$  from Eq. (3): assuming that the Fermi velocity  $v_F$  is of the order of  $10^6$  m/s as in classical metals, we get  $\tau_1 \approx 0.018$  ps for

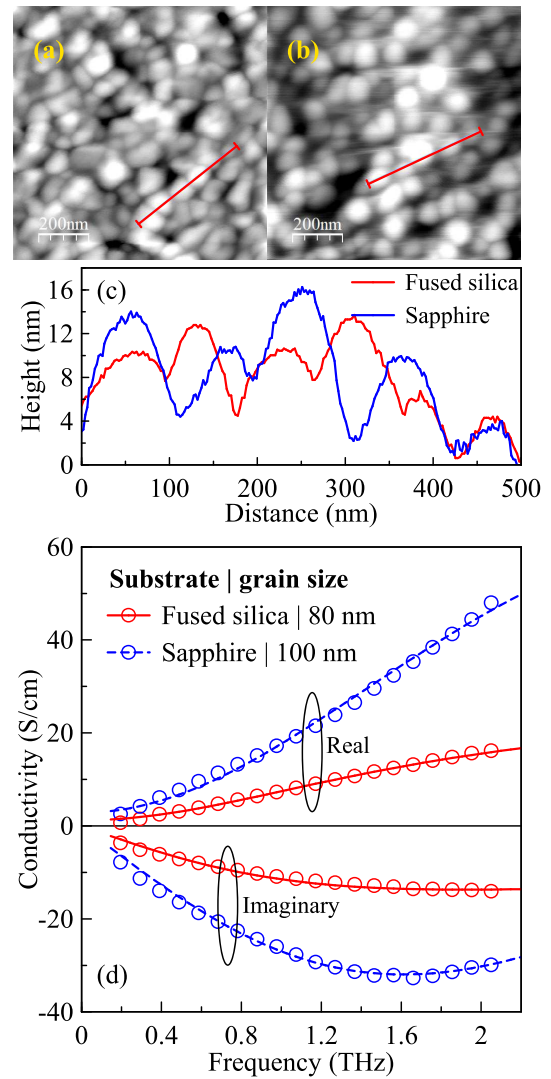


FIG. 9. Atomic force microscopy image of the surface of the PY-CCO film ( $y = 16\%$ ) deposited on (a) fused silica and (b) sapphire substrate. The grain size of the film deposited on the fused silica ( $\sim 80$  nm) is smaller than of that on the sapphire substrate ( $\sim 100$  nm). (c) Height profile along the red lines. (d) Terahertz conductivity of these films in the metallic state ( $T = 175$  K). Symbols: measured data. Lines: fits using the modified Drude-Smith model; the pertinent parameters are  $\sigma_1 = 26$  S/cm,  $\theta_1 = 0.09$  ps,  $c_1 = -0.95$  (fused silica substrate) and  $\sigma_1 = 130$  S/cm,  $\theta_1 = 0.04$  ps,  $c_1 = -0.98$  (sapphire substrate).

films on fused silica substrate and  $\tau_1 \approx 0.04$  ps for films on sapphire substrate; these values are shorter than the values  $\tau_1$  and  $\tau_2$  found for the bulk ceramics, which can be attributed to the additional scattering caused by the grain boundaries. Note also that the amplitudes of  $\sigma_1$  are correlated with the values of  $\tau_1$ , consistently with the Drude picture of charge transport.

In Fig. 10 we demonstrate the relation of dc, microwave and THz conductivities. The higher is the radiation frequency, the shorter is the distance over which the charge transport is probed. Using the THz radiation, we thus reveal the transport inside the grains (which—as we demonstrated—is still strongly affected by the grain boundaries); in this case,

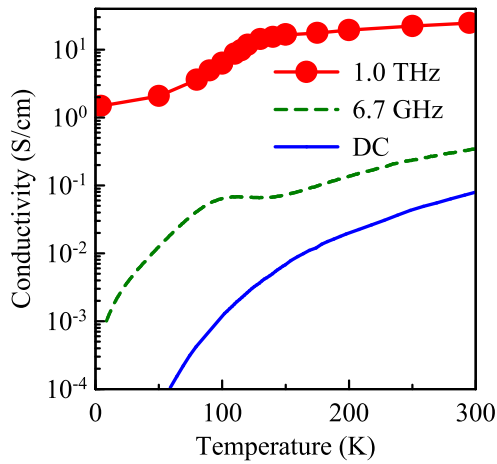


FIG. 10. Temperature dependencies of the dc, microwave and THz conductivities of the PYCCO ( $y = 16\%$ ) nanogranular film on sapphire substrate.

we still see a clear manifestation of the phase transition. Using microwave radiation, we probe considerably longer distances (roughly by a factor of  $\sqrt{f_{\text{THz}}/f_{\text{GHz}}}$  [30] which is around 10 in our case, thus involving several grains and grain boundaries). As expected, the microwave conductivity level is between the dc and THz conductivity. Although the response exhibits features correlating with the temperature dependence of the THz conductivity, it would be almost impossible to infer on the character of the phase transition based solely on the microwave conductivity. The dc conductivity finally represents a long-range transport, along a macroscopic distance. The charges are transported not only within grains but also through a large number of grain boundaries. The result show that the long-range transport is fully controlled by highly resistive grain boundaries, with completely no influence of the metal-insulator transition occurring in the grain interior.

#### D. Conductivity of nanogranular films

The terahertz conductivity spectra of the thick nanogranular films illustrated in Figs. 11 and 12 show that a pronounced change in the conductivity amplitude and spectrum occurs for the doped compounds ( $y \neq 0$ ), whereas the variation of conductivity is weaker in the case of the undoped material ( $y = 0$ ).

For the analysis of the conductivity spectra, we employed a model containing a single modified Drude-Smith term. The spectra can be well described assuming that the lattice response  $\epsilon_p$  and the back-scattering coefficient  $c_1$  are temperature-independent parameters; the temperature dependence of the remaining parameters is shown in Fig. 13 for all samples. We recall that the scattering time  $\tau_1$  controls namely the rate of decrease of the conductivity at frequencies well above our accessible spectral range, therefore its accuracy is poor (we can only conclude that  $\tau_1$  is at most a few tens of femtoseconds).

In the undoped material ( $y = 0$ ), the conductivity amplitude  $\sigma_1$  is rather high for all temperatures, and it only weakly increases upon heating. The only pronounced change of charge transport parameters occurs below 100 K for the

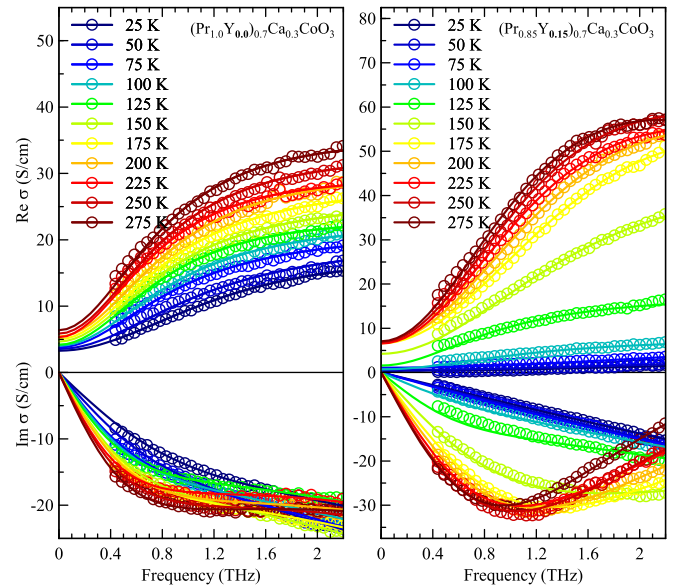


FIG. 11. Examples of terahertz conductivity spectra of undoped ( $y = 0$ ) and yttrium-doped ( $y = 15\%$ )  $(\text{Pr}_{1-y}\text{Y}_y)_{0.7}\text{Ca}_{0.3}\text{CoO}_3$  films (left and right panel, respectively) on sapphire substrates. Symbols: measured data, lines: fit using the modified Drude-Smith model and lattice response  $\epsilon_p$ .

diffusion time  $\theta_1$ . Since the grain size (representing the confinement length) is temperature independent and  $\sigma_1$  (and therefore also  $\tau_1$ ) is almost constant below 100 K, Eq. (3)

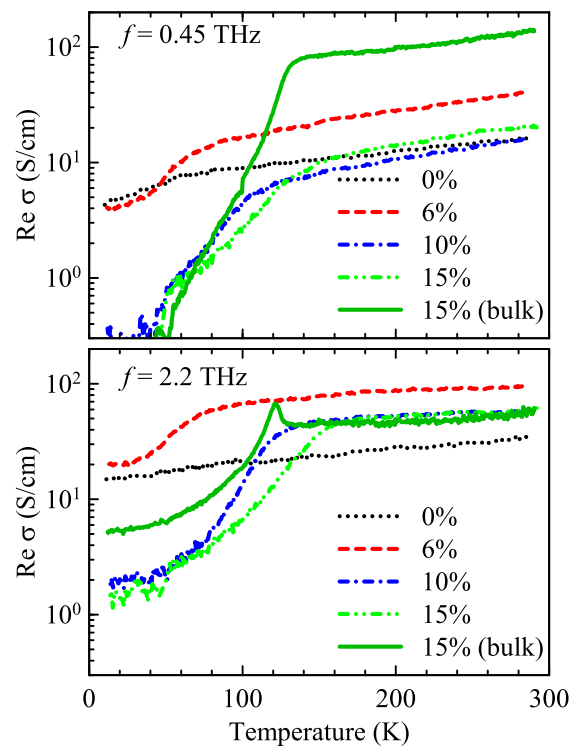


FIG. 12. Temperature dependence of the terahertz conductivity of the investigated  $(\text{Pr}_{1-y}\text{Y}_y)_{0.7}\text{Ca}_{0.3}\text{CoO}_3$  films compared with the response of the  $15 \mu\text{m}$  thick bulk ceramics, for frequencies on the borders of the accessible spectral range.

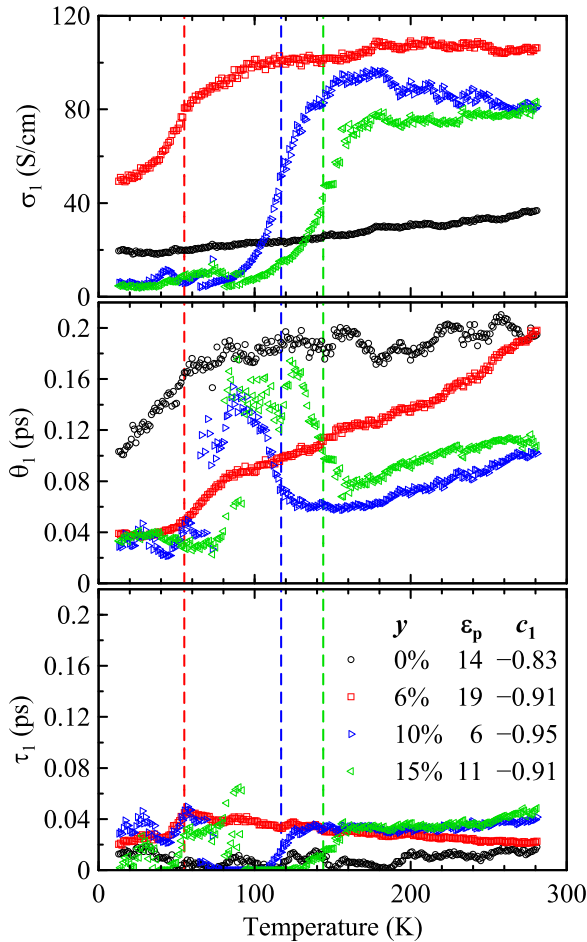


FIG. 13. Summary of fitting parameters of the modified Drude-Smith model for the nanogranular films on sapphire substrate. The vertical dashed lines indicate the temperatures around the largest slope of  $\sigma_1$ . The parameters  $c_1$  and  $\epsilon_p$  are provided only for completeness; their accuracy is not sufficient to allow drawing any conclusions about their dependence on the doping  $y$ .

implies that the Fermi velocity slightly increases from 100 toward 10 K.

The conductivity amplitude  $\sigma_1$  in the doped cobaltites ( $y \neq 0$ ) exhibits a pronounced increase associated with the insulator to metal transition (as it could be anticipated already from the bare spectra). The transition temperature increases with increasing doping content. The onset of the increase in  $\sigma_1$  is accompanied also by a complex temperature dependence of  $\theta_1$ .

In contrast to the ceramics, the THz conductivity of the thick nanogranular films in the metallic state is considerably suppressed due to the confinement of charges by grain boundaries. This means that possible changes in the spectra (the red shift of the excitation eigenfrequency upon heating) are almost invisible in the case of the nanogranular films; they cause only subtle changes in the spectral shape which appear as the complex behavior in the temperature dependence of  $\theta_1$ . The parameter containing the essential quantitative information on the phase transition is thus the conductivity amplitude  $\sigma_1$ .

To summarize: grain boundaries in the PYCCO films fundamentally reduce the efficiency of the charge transport and

prevent observation of the metal-insulator phase transition in the dc conductivity. Nevertheless, the metal-insulator phase transition is preserved in the interior of the 100-nm sized grains, and it can be resolved and analyzed using THz radiation.

#### IV. INFRARED SPECTRA

The results on bulk ceramics as well as on nanogranular films indicate that an excitation shifting toward the infrared region is present at least in the vicinity of the metal-insulator phase transition. For this reason, we systematically investigated also the infrared reflectivity spectra using Fourier-transform infrared spectroscopy, which captures the combined response of lattice dynamics (phonons) and free charges.

In the metallic phase of the ceramics, the reflectivity is featureless and high [Fig. 14(a)], due to the dominating response of free charges. Upon cooling, the conductivity (and therefore also the overall reflectivity) decreases, therefore we observe a series of spectral features due to phonon modes which are no longer screened by the conductivity. The *Pnma* structure contains 4 molecules of PYCCO; a group analysis shows that there are in total 25 infrared active phonon modes. We can see only a small subset of these modes in the accessible spectral range; this indicates that some of the features are in fact close modes overlapping each other (overlapping modes would for example explain the broad features around 9 THz). Nevertheless, fitting the reflectivity spectra using a sum of six oscillators plus a single-term of the modified Drude-Smith model provides a good insight into the behavior of the phonon modes [Fig. 14(b)]. Except for the lowest mode with frequency 6.1 THz, all other modes soften upon heating (at least up to 150 K). This is particularly pronounced and directly visible in the reflectivity spectra for the mode starting at 14.6 THz which red-shifts by more than 1 THz at 140 K.

The phonon softening upon heating reflects the large expansion change in the lattice constant [11]. Since we do not observe any abrupt change in the phonon frequencies, we conclude that the phase transition is not accompanied by discontinuous structural changes or redistribution of bound charges. There is also no indication of a presence of further phonon modes below 4 THz.

The behavior of the phonon modes in the metallic phase was investigated on the nanogranular films (Fig. 15) which—due to their lower conductivity—favor the interaction of the infrared radiation with phonons. The nanogranular film exhibits qualitatively similar features as the ceramics, but they are considerably broader which indicates that the crystal of the grains may be rather defective. Nevertheless, at least the lowest phonon frequency can be obtained from the fit accurately, and we observed that above phase transition it gradually and considerably red-shifts with increasing temperature. Note that the probing radiation here has high enough frequency to marginalize a possible influence of the confinement.

The remaining question regards the absence of the excitation resolved in Sec. III in any of the measured infrared reflectivity spectra. In fact, the amplitude of the excitation is too weak and the sensitivity of the reflectivity spectra is too low to permit the observation of this feature. Note that already

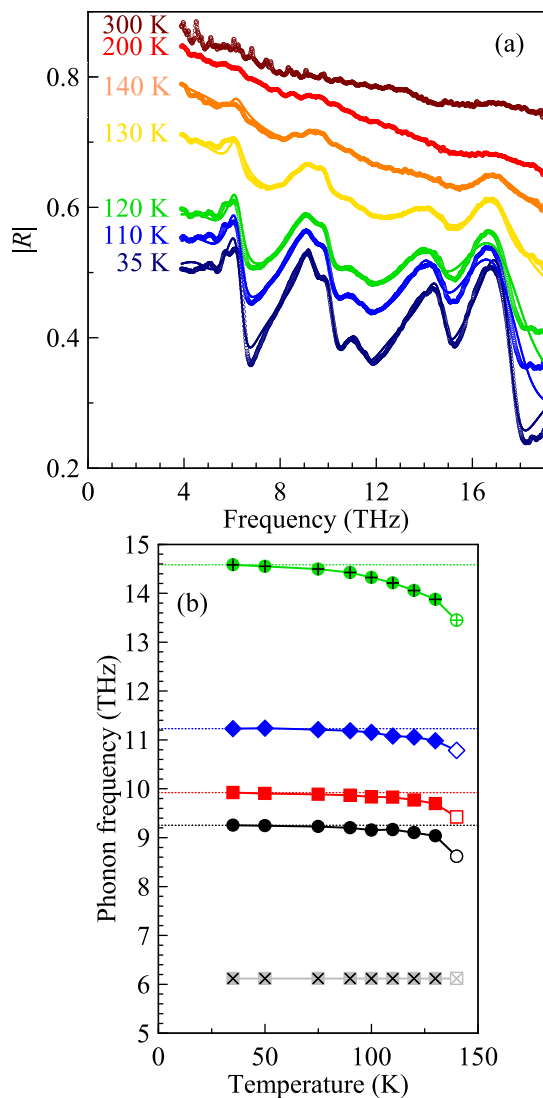


FIG. 14. (a) Examples of infrared reflectivity spectra of PYCCO ( $y = 15\%$ ) ceramics. Symbols: measured data, lines: fit. (b) Temperature-dependence of the phonon mode frequencies determined from the fit of the infrared reflectivity spectra. The accuracy of the last point ( $T = 140$  K) is limited as the phonons are only poorly resolved above this temperature. The horizontal dotted lines serve to emphasize the softening (frequency decrease) of the phonon modes with increasing temperature.

in the insulating state, the reflectivity is rather elevated (above 50%), which contributes to a substantial screening of any possible spectral features. Furthermore, the Fresnel reflection coefficient is controlled by refractive index, or equivalently, by permittivity: since conductive contribution  $\sigma$  translates into the permittivity as  $i\sigma/(2\pi f\epsilon_0)$ , it becomes suppressed as we approach the higher frequencies. Presence of such a weak excitation in the infrared spectra may be then easily masked by systematic measurement errors such as etalon effects.

## V. CONCLUSIONS

The evolution of the metal-insulator transition in mixed-valence cobaltites ( $\text{Pr}_{1-y}\text{Y}_y$ ) $_{0.7}\text{Ca}_{0.3}\text{CoO}_3$  ( $0 \leq y \leq 15\%$ )

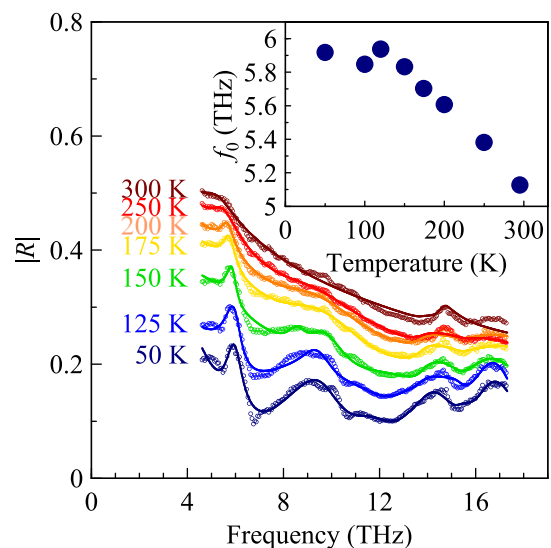


FIG. 15. Examples of infrared reflectivity spectra of PYCCO ( $y = 6\%$ ) nanogranular film on fused silica. Symbols: measured data, lines: fit. Inset: Temperature-dependence of the lowest phonon frequency determined from the fit.

was investigated up to terahertz and infrared frequencies. Samples with special thicknesses (15  $\mu\text{m}$  for the bulk ceramics, 4–6  $\mu\text{m}$  for the nanogranular films) were prepared to enable the measurement of the terahertz conductivity both in the insulating and metallic state on the same sample.

In yttrium-doped bulk ceramics, we observed that the phase transition cannot be explained as a simple variation in the density of free charge carriers, or even more generally, as a cross-over from insulating to metallic state. Instead, we revealed a temperature-dependent excitation which red-shifts upon transition from the insulating to the metal state. The spectrum of this excitation resembles a broad resonance; its presence is further clearly manifested by a sharp peak in the temperature dependence of the real part of THz conductivity at higher frequencies. We interpret this excitation as a consequence of charge motion in a complex potential landscape, which changes from tightly bound charges in the insulating phase to almost free charges in the metallic phase (Fig. 8). In the metallic state, a small fraction of free charges exhibits a long scattering time ( $>0.44$  ps) which is an extraordinary value with regard to the dirty nature of the sample; this further implies a strong frequency dependence of the scattering time already from sub-THz frequencies. A more detailed interpretation of the phase transition as well as of the response in the metallic state thus clearly requires a further theoretical research.

The metal-insulator transition occurs also in the yttrium-doped nanogranular films. A characteristic increase of the conductivity with increasing temperature was observed at terahertz frequencies, which probe the conductivity inside the grains. The effect of the charge confinement is substantial even at these high frequencies; the evolution of the potential landscape in which charges move thus appears only as a subtle change in the parameters of the modified Drude-Smith model. The conductivity at lower frequencies (gigahertz spectral range) still exhibits certain indications of the phase transition;

however, the role of the resistive grain boundaries is already too significant to permit a quantitative characterization of the transport properties. The dc conductivity is limited by highly resistive grain boundaries; in turn, dc measurements are not able to monitor or even provide any hints about the metal-insulator phase transition. Terahertz spectroscopy thus proved to be of ultimate importance for the investigation of transport properties in materials with complex morphology.

The phase transition from insulating to the metal state is also accompanied by a weak softening of phonon modes, which reflects the expansion of lattice parameters.

It is interesting to note that the conductivity amplitude in the nanogranular film ( $\sigma_1$ ) reaches almost one third of the conductivity amplitude in the bulk ceramics (which can be approximately represented by the sum  $\sigma_1 + \sigma_2$ ). This means that the quality of the grain interiors of the nanogranular films prepared by chemical methods is well comparable to that of the bulk material, while the

long-range transport properties are compromised by resistive grain boundaries.

The presented work also clearly demonstrates the double advantage of terahertz spectroscopy: the possibility to investigate grain interiors (and thus to understand the phase transition dynamics in the nanogranular films where dc conductivity does not provide useful information), and the ability to resolve pertinent part of conductivity spectra which encode details about the phase transition dynamics.

#### ACKNOWLEDGMENTS

We acknowledge the financial support by the Czech Science Foundation (Project No. 17-04412S), and by Operational Program Research, Development and Education financed by European Structural and Investment Funds and the Czech Ministry of Education, Youth and Sports (Project No. SOLID21-CZ.02.1.01/0.0/0.0/16\_019/0000760).

- 
- [1] I. Terasaki, S. Shibusaki, S. Yoshida, and W. Kobayashi, *Materials* **3**, 786 (2015).
- [2] S. Maekawa, T. Tohyama, S. E. Barnes, S. Ishihara, W. Koshibae, and G. Khaliullin, *Physics of Transition Metal Oxides* (Springer-Verlag, Berlin, 2004).
- [3] Y. Noda, H. Fujishiro, T. Naito, A. Ito, T. Goto, J. Hejtmanek, and Z. Jirak, *AIP Adv.* **6**, 025318 (2016).
- [4] A. Gulec, D. Phelan, C. Leighton, and R. F. Klie, *ACS Nano* **10**, 938 (2016).
- [5] T. Naito, H. Fujishiro, T. Nishizaki, N. Kobayashi, J. Hejtmánek, K. Knížek, and Z. Jiráček, *J. Appl. Phys.* **115**, 233914 (2014).
- [6] P. Novák, K. Knížek, M. Maryško, Z. Jiráček, and J. Kuneš, *J. Phys.: Condens. Matter* **25**, 446001 (2013).
- [7] K. Knížek, Z. Jiráček, P. Novák, and C. de la Cruz, *Solid State Sci.* **28**, 26 (2014).
- [8] Z. Jiráček, J. Hejtmánek, K. Knížek, M. Maryško, P. Novák, E. Šantavá, T. Naito, and H. Fujishiro, *J. Phys.: Condens. Matter* **25**, 216006 (2013).
- [9] J. Hejtmánek, E. Šantavá, K. Knížek, M. Maryško, Z. Jiráček, T. Naito, H. Sasaki, and H. Fujishiro, *Phys. Rev. B* **82**, 165107 (2010).
- [10] J. Hejtmánek, Z. Jiráček, O. Kaman, K. Knížek, E. Šantavá, K. Nitta, T. Naito, and H. Fujishiro, *Eur. Phys. J. B* **86**, 305 (2013).
- [11] K. Knížek, J. Hejtmánek, M. Maryško, P. Novák, E. Šantavá, Z. Jiráček, T. Naito, H. Fujishiro, and C. de la Cruz, *Phys. Rev. B* **88**, 224412 (2013).
- [12] J. L. García-Munoz, C. Frontera, A. J. Barón-González, S. Valencia, J. Blasco, R. Feyerherm, E. Dudzik, R. Abrudan, and F. Radu, *Phys. Rev. B* **84**, 045104 (2011).
- [13] H. Fujishiro, T. Naito, S. Ogawa, N. Yoshida, K. Nitta, J. Hejtmánek, K. Knížek, and Z. Jiráček, *J. Phys. Soc. Jpn.* **81**, 064709 (2012).
- [14] K. Knížek, J. Hejtmánek, P. Novák, and Z. Jiráček, *Phys. Rev. B* **81**, 155113 (2010).
- [15] R. Ulbricht, E. Hendry, J. Shan, T. F. Heinz, and M. Bonn, *Rev. Mod. Phys.* **83**, 543 (2011).
- [16] H. Němec, P. Kužel, and V. Sundström, *J. Photochem. Photobiol. A* **215**, 123 (2010).
- [17] K. S. Kumar, G. L. Prajapati, R. Dagar, M. Vagadia, D. S. Rana, and M. Tonouchi, *Adv. Opt. Mater.* **8**, 1900958 (2019).
- [18] T. L. Cocker, L. V. Titova, S. Fourmaux, G. Holloway, H.-C. Bandulet, D. Brassard, J.-C. Kieffer, M. A. El Khakani, and F. A. Hegmann, *Phys. Rev. B* **85**, 155120 (2012).
- [19] A. N. Hattori, Y. Fujiwara, K. Fujiwara, T. V. A. Nguyen, T. Nakamura, M. Ichimiya, M. Ashida, and H. Tanaka, *Nano Lett.* **15**, 4322 (2014).
- [20] H. Fujishiro, Y. Noda, K. Akuzawa, T. Naito, A. Ito, T. Goto, M. Maryško, Z. Jirak, J. Hejtmanek, and K. Nitta, *J. Appl. Phys.* **121**, 115104 (2017).
- [21] V. Skoromets, C. Kadlec, J. Drahekoupil, J. Schubert, J. Hlinka, and P. Kužel, *Phys. Rev. B* **89**, 214116 (2014).
- [22] V. Skoromets, H. Němec, J. Kopeček, P. Kužel, K. Peters, D. Fattakhova-Rohlfing, A. Vetushka, M. Müller, K. Ganzerová, and A. Fejfar, *J. Phys. Chem. C* **119**, 19485 (2015).
- [23] P. F. Henning, C. C. Homes, S. Maslov, G. L. Carr, D. N. Basov, B. Nikolić, and M. Strongin, *Phys. Rev. Lett.* **83**, 4880 (1999).
- [24] H. Němec, P. Kužel, and V. Sundström, *Phys. Rev. B* **79**, 115309 (2009).
- [25] E. Hendry, M. Koeberg, B. O'Regan, and M. Bonn, *Nano Lett.* **6**, 755 (2006).
- [26] H.-K. Nienhuys and V. Sundström, *Appl. Phys. Lett.* **87**, 012101 (2005).
- [27] H. Němec, V. Zajac, I. Rychetský, D. Fattakhova-Rohlfing, B. Mandlmeier, T. Bein, Z. Mics, and P. Kužel, *IEEE Trans. Terahertz Sci. Technol.* **3**, 302 (2013).
- [28] T. L. Cocker, D. Baillie, M. Buruma, L. V. Titova, R. D. Sydora, F. Marsiglio, and F. A. Hegmann, *Phys. Rev. B* **96**, 205439 (2017).
- [29] J. Mrozek and H. Němec, *Phys. Rev. B* **86**, 075308 (2012).
- [30] P. Kužel and H. Němec, *Adv. Opt. Mater.* **8**, 1900623 (2020).
- [31] F. Gervais, *Mater. Sci. Eng. R* **R39**, 29 (2002).
- [32] V. Bovtun, V. Pashkov, M. Kempa, S. Kamba, A. Eremenko, V. Molchanov, Y. Poplavko, Y. Yakymenko, J. H. Lee, and D. G. Schlom, *J. Appl. Phys.* **109**, 024106 (2011).

- [33] V. Bovtun, S. Veljko, A. Axelsson, S. Kamba, N. Alford, and J. Petzelt, *Integr. Ferroelectr.* **98**, 53 (2008).
- [34] J. Krupka, *Meas. Sci. Technol.* **17**, R55 (2006).
- [35] A. Pashkin, M. Kempa, H. Němec, F. Kadlec, and P. Kužel, *Rev. Sci. Instrum.* **74**, 4711 (2003).
- [36] L. Duvillaret, F. Garet, and J.-L. Coutaz, *IEEE J. Sel. Top. Quantum Electron.* **2**, 739 (1996).
- [37] F. A. Hegmann, O. Ostroverkhova, and D. G. Cooke, *Photophysics of Molecular Materials* (Wiley-VCH Verlag GmbH & Co. KGaA, Weinheim, 2006), chap. 7, pp. 367–428.
- [38] T. Ostatnický, V. Pushkarev, H. Němec, and P. Kužel, *Phys. Rev. B* **97**, 085426 (2018).
- [39] N. V. Smith, *Phys. Rev. B* **64**, 155106 (2001).
- [40] R. H. Lyddane, R. G. Sachs, and E. Teller, *Phys. Rev.* **59**, 673 (1941).
- [41] D. N. Basov, R. D. Averitt, D. van der Marel, M. Dressel, and K. Haule, *Rev. Mod. Phys.* **83**, 471 (2011).
- [42] M. van Exter and D. Grischkowsky, *Appl. Phys. Lett.* **56**, 1694 (1990).
- [43] H. Němec, K. Knížek, Z. Jiráček, J. Hejtmánek, M. Soroka, and J. Buršík, *J. Phys.: Condens. Matter* **28**, 355601 (2016).